JOURNAL OF GEOPHYSICAL RESEARCH, VOL. 114, A07209, doi:10.1029/2008JA014007, 2009

Simultaneous ground-satellite optical observations of postnoon shock aurora in the Southern Hemisphere

T. Motoba,[1] A. Kadokura,[1] Y. Ebihara,[2] H. U. Frey,[3] A. T. Weatherwax,[4] and N. Sato[1]

Received 22 December 2008; revised 23 April 2009; accepted 29 April 2009; published 9 July 2009.

[1] On 14 June 2005, a transient postnoon shock aurora, induced by an interplanetary (IP) shock, was observed simultaneously with the FUV imager onboard the IMAGE satellite and the all-sky imager (ASI) at the South Pole Station (−74.3° magnetic latitude (MLAT), ∼15 magnetic local time). The global evolution of the shock aurora was identified by the FUV, whereas the detailed spatial-temporal structure was identified by the ASI. Both optical emissions for the shock aurora showed a reasonable agreement in a common field of view. During the transient auroral brightenings in the dayside oval detected by the FUV, a two-step development of the shock aurora was identified by the ASI in the afternoon sector of the oval. Just after the IP shock, the ASI first observed a diffuse 557.7 nm aurora expanding duskward at the equatorward edge of the oval (−70° to −73° MLAT). About 5 min later, new discrete auroral forms (arcs) were detected in the middle of the oval (−73° to −76° MLAT) by both 557.7 nm and 630.0 nm ASI images. The discrete arcs developed with relatively brighter emissions, and had a lifetime of the order of 10 min, during the main impulse (MI) of geomagnetic sudden commencement. The spectrographic auroral imagers onboard the IMAGE satellite indicated that proton precipitation played an effective role in the first shock auroral emission observed with the ASI, while intense electron precipitation played an effective role in the second one. Mechanisms of the first and second postnoon shock auroras presented here are speculated to be associated with the wave-particle interaction process, and the field-aligned acceleration process in the region of the MI-related upward field-aligned currents, respectively.

Citation: Motoba, T., A. Kadokura, Y. Ebihara, H. U. Frey, A. T. Weatherwax, and N. Sato (2009), Simultaneous ground-satellite optical observations of postnoon shock aurora in the Southern Hemisphere, *J. Geophys. Res.*, *114*, A07209, doi:10.1029/2008JA014007.

1. Introduction

[2] Interplanetary (IP) shock and a sudden solar wind dynamic pressure (Psw) change can cause transient auroral emissions (often referred as "shock aurora") developing on a global scale [*Vorobyev*, 1974; *Craven et al.*, 1986; *Spann et al.*, 1998; *Zhou and Tsurutani*, 1999; *Meurant et al.*, 2003, 2004; *Liou et al.*, 2007; *Laundal and Østgaard*, 2008]. Generally, just after the arrival of an IP shock on the dayside magnetopause, the initial brightening of shock aurora appears around the noon cusp region. After that, within a few or several minutes the shock aurora expands longitudinally to dawn and/or dusk sectors and eventually reaches the nightside sector. Several possible mechanisms for the shock aurora were suggested (for more details, see *Tsurutani et al.* [2001], *Liou et al.* [2002], and *Zhou et al.* [2003]); adiabatic compression, reductions in the mirror ratio, field-aligned current acceleration, viscous interaction, and so on. It has been expected that each mechanism causes different types of shock aurora. For example, in the cases of adiabatic compression, reductions in the mirror ratio, and viscous interaction, the diffuse-type auroras are caused by precipitation of preexisting/trapped particles entering the loss cone as a result of the magnetic field and plasma compression of the outer magnetosphere. This process could be performed by varying either the loss cone or the particle pitch angles. In contrast, the field-aligned current acceleration is responsible for discrete-type auroras.

[3] The satellite optical data are very useful for identifying temporal and spatial evolution of shock aurora on a global scale. The global view of shock aurora from the satellite optical instruments indicated two different responses, rapid and slower responses. The former appears almost simultaneously (within a few minutes) from noon to the nigh after the arrival of IP shock on the magnetopause [*Chua et al.*, 2001]. The rapid response could be linked with the interaction with fast-mode wave propagating at speed of the order of 1000 km/s in the magnetosphere [e.g., *Moore et al.*, 1987], launched by IP shock. In the latter case, on the

[1]National Institute of Polar Research, Tokyo, Japan.
[2]Institute for Advanced Research, Nagoya University, Nagoya, Japan.
[3]Space Sciences Laboratory, University of California, Berkeley, California, USA.
[4]Department of Physics, Siena College, Loudonville, New York, USA.

0148-0227/09/2008JA014007$09.00

other hand, the auroral emissions propagate from noon to dawn and/or dusk directions with 6–11 km/s in the polar ionosphere [*Zhou and Tsurutani*, 1999]. The propagation speed in the polar ionosphere is roughly comparable to that in the magnetosheath. The slower response could be associated with the compressed magnetospheric state due to sweeping of IP shock along the flanks of the magnetopause. However, because of the low spatial resolution of the satellite optical instruments, it is difficult to discriminate definitely whether the shock aurora is discrete-type or diffuse-type.

[4] The shock auroral forms can frequently be identified by the precipitating particle observations on in situ polar orbiting satellites at low altitudes. In addition, direct observations of the auroral particle precipitation can provide also important information concerning where their sources map in the equatorial plane. Some previous studies have indicated that a major source of shock auroras is precipitation of unstructured electrons, originating from the central plasma sheet [*Liou et al.*, 2007]. *Zhou et al.* [2003] demonstrated that there are two different precipitation structures for the shock auroras; one is precipitation of low-energy structured electrons ($<\sim$1 keV) poleward of the auroral oval, the other precipitation of high-energy unstructured electrons ($\sim$1–10 keV) equatorward. In general, it has been believed that the structured (unstructured) electron precipitation leads to the discrete (diffuse) auroral form. However, because of the limited satellite passes across the polar ionosphere just during shock auroras, it is difficult to reveal how the shock auroral forms evolve in time and space. In order to do that, high temporal and spatial resolution ground-based optical data would be essential.

[5] Ground-based optical observations for dayside shock aurora were frequently performed on Svalbard, Norway [*Sandholt et al.*, 1985, 1994; *Kozlovsky et al.*, 2005]. These studies also indicated a sudden intensification of the dayside auroral emission around noon cusp after the arrival of IP shock, in the same manner as the satellite-based optical measurements described above. Using simultaneous optical observations from ground and space which are very rare for dayside shock aurora, *Kozlovsky et al.* [2005] observed Psw-induced rayed arcs appearing from the poleward edge of the prenoon auroral oval. They suggested two possible mechanisms (one is based on the phase difference between the field line resonance oscillations on neighboring L shells, the other on the ''interchange instability''), in order to explain the origin of the auroral arcs observed in prenoon. However, since the previous ground-based studies tended to focus on the shock auroral features around the noon cusp/cleft region, it is still unclear where and how shock auroral forms behave on the dayside.

[6] All-sky imager (ASI) used in this study has been operated at the South Pole Station (SPA, magnetic latitude (MLAT) = -74.3°, magnetic local time (MLT) = UT-3.5 h) during the austral winter season since 1997. (Details for specification of the ASI improved in 2002 were described by *Ebihara et al.* [2007].) The available wavelengths of the ASI are 557.7, 630.0, 427.8, 589.0 and 486.1 nm. Like Svalbard in the Northern Hemisphere, SPA is a very unique location in the Southern Hemisphere for continuous ground-based optical observations of the dayside auroral emissions. The most significant advantage is that the auroral emissions are detectable at all MLTs during the austral winter season because the Sun is 12° below the horizon for about 4 months (this means that SPA is almost or completely darkness on the dayside). The ASI field of view on the dayside covers from the auroral zone to the polar cap, including the cusp, while on the nightside it covers around the poleward boundary of the auroral zone. In addition, the sky conditions over SPA, which are critical for ground-based optical observations, are mostly clear.

[7] In this paper, we report a shock aurora event observed simultaneously by both ground and satellite optical instruments in the Southern Hemisphere on 14 June 2005. The simultaneous ground-satellite optical observations give a unique opportunity to examine the detailed structure of the dayside shock aurora. Ground optical images of the shock aurora were identified by the ASI at SPA, while satellite optical images by the far ultraviolet (FUV) cameras [*Mende et al.*, 2000] on board the IMAGE (Imager for Magnetopause-to-Aurora Global Exploration) satellite. In addition to global evolution of the shock aurora shown by the IMAGE-FUV, we present different temporal and spatial behavior of discrete and diffuse emissions for the shock aurora.

2. Observations

2.1. Solar Wind Conditions

[8] Figure 1 indicates solar wind conditions detected by the ACE satellite during the interval 1400–2000 UT on 14 June 2005. The first, second, third, and fourth panels are the three components of the interplanetary magnetic field (IMF), and solar wind plasma parameters including the solar wind velocity (Vsw), the density (Nsw), and the dynamic pressure (Psw), respectively. The temporal resolutions of the ACE magnetic and plasma data are 16 s and 64 s, respectively. The fifth panel shows the SYM-H index [*Iyemori*, 1990] with 1-min time resolution during the same interval. The SYM-H index measures the mean longitudinally symmetric component of the magnetic disturbances, averaged from six globally distributed magnetometers at middle latitudes.

[9] For the 5 h preceding the IP shock, the Bz and By components of IMF were positive in the range of 0.0 nT to 5.0 nT. These IMF conditions were reflected in the quiet geomagnetic conditions; AE index was less than 250 nT and 3-h Kp index of 1 or 2 (not shown). Since about 40 min before the onset of the IP shock, the Bz component was very weakly negative (values between 0.0 nT and -1.0 nT). At $\sim$1754 UT (marked by dashed vertical line in Figure 1), ACE recorded the IP shock, identified by sharp increases in Vsw (from 443 km/s to 524 km/s), Nsw (from 7.1/cc to 13.5/cc) and Psw (from 2.3 nPa to 6.2 nPa). At the same time, the IMF By suddenly changed by over 10 nT, while the IMF Bx and Bz were essentially unaffected by the IP shock. The propagation speed of the IP shock estimated by using the magnetic coplanarity method [*Colburn and Sonett*, 1966] and the conservation of mass flux was $\sim$590 km/s. When the IP shock arrived at the dayside magnetopause, it caused a geomagnetic sudden commencement (SC) on the ground, as identified by a sudden increase in the SYM-H index at 1835 UT. The SC amplitude of the SYM-H index was 32 nT.

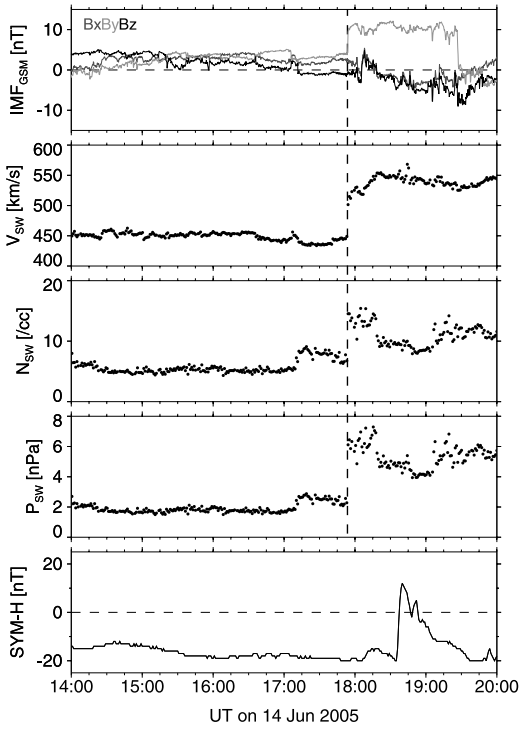

Figure 1. Solar wind magnetic field and plasma data recorded by the ACE satellite on 14 June 2005 from 1400 to 2000 UT. The first, second, third, and fourth panels are the three components of interplanetary magnetic field (IMF) in the GSM coordinate system, the solar wind speed (Vsw), the density (Nsw), and the dynamic pressure (Psw), respectively. The fifth panel is the SYM-H index.

[10] About 7 min (1803 UT) after the onset of IP shock, ACE detected a transient IMF Bz change from −1.0 nT to −3.0 nT, but immediately the IMF Bz turned northward at ∼1806 UT. At ∼1818 UT, the IMF Bz turned southward again, but slowly. In this study, therefore our attention is focused on the interval (corresponding to the interval ∼1835–1855 UT on the Earth) when the IMF effects on the dayside ionosphere were relatively weak or mostly negligible.

2.2. Ground Magnetometer and Photometer

[11] Figure 2 shows the time series of the H component of magnetic field at SPA and of the photometer of both 427.8 nm and 630.0 nm wavelengths at SPA during the interval 1830–1900 UT, together with the H component of magnetic field at Kakioka (KAK, 27.37° MLAT, MLT = UT+9 h). Time resolution of both magnetometer and photometer data at SPA is 10 s, while at KAK 1 s. The 427.8 nm and 630.0 nm wavelengths represent the auroral emissions from ionized molecular nitrogen (blue) and atomic oxygen (red), respectively.

[12] The SC signature seen in the SYM-H index is identified also by the H component at KAK. The more accurate SC onset time determined by the 1-s sampling data at KAK was 1835:25 UT (shown by vertical line in Figure 2). This onset time was used as an indication of the arrival of the IP shock at the Earth. The stepwise change in the H component at KAK reached a peak (amplitude of ∼20 nT) before 1840 UT, and then the amplitude remained almost the stable value around 20 nT.

[13] After the SC onset, the H component of magnetic field at SPA was followed by two successive impulses: the first impulse was negative, and the second one positive. The negative and positive impulses correspond to preliminary and main impulses (referred as PI and MI) of SC in the afternoon auroral zone [*Araki*, 1994], respectively. In our case, the MI signal began around 1840 UT, and the MI decayed after ∼1850 UT, according to the magnetometer data from a southern polar cap station near local noon (not shown). This is consistent with the fact that the MI signature in the polar ionosphere has a lifetime of the order from several to 10 min. The negative/positive magnetic fluctuation seen after ∼1844 UT could be attributed to localized disturbances superposed on the MI.

[14] During the PI (within ∼5 min after the SC onset), the intensity at 427.8 nm gradually increased from 0.1 kR to 0.25 kR. In contrast, the intensity at 630.0 nm was almost steady around 0.1 kR. At the beginning of MI around 1840 UT, both intensities were suddenly enhanced. Between 1840 UT and 1842 UT, the intensity at 427.8 nm (0.3–1.0 kR) was much larger than that at 630.0 nm (0.1∼0.45 kR). In addition, the risetime of 427.8 nm emission was very sharp and the intensity reached a peak (∼1.0 kR) within 1 min. In contrast, it took ∼2 min for the risetime of 630.0 nm emission to reach a peak (∼0.45 kR). The different risetime between both emissions could be dependent on each radiative lifetime. Between 1842 UT and 1850 UT, both intensities were almost the same (0.4–0.5 kR). Around the end of MI (between 1850 and 1854 UT), only the intensity at 427.8 nm was reduced by ∼0.2 kR. Between 1854 and 1858 UT the intensity was enhanced by ∼0.6 kR again.

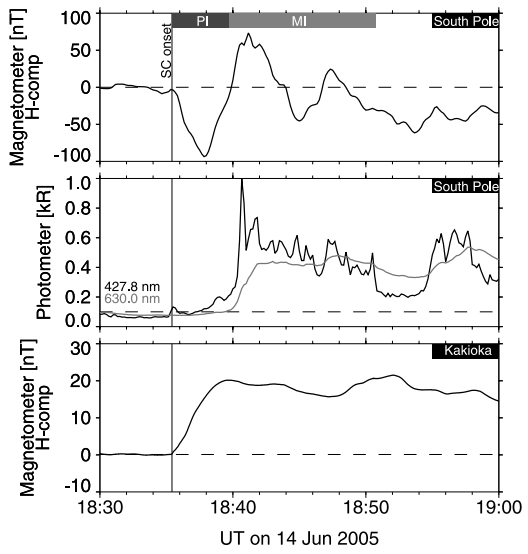

Figure 2. (top) Time series of the magnetic H component at the South Pole Station (SPA), (middle) the 427.8 nm (black curve) and 630.0 nm (gray curve) emissions detected by the photometer at SPA, and (bottom) the magnetic H component at Kakioka. Vertical line in each plot is at the time of the SC onset.

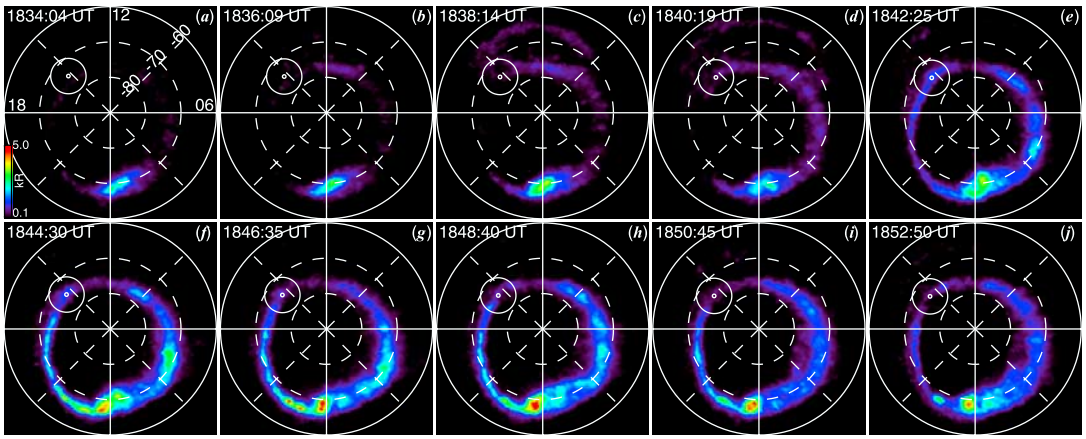

Figure 3. Sequence of WIC images from the Southern Hemisphere displayed into a magnetic latitude/MLT grid with local noon at the top, midnight at the bottom, and dawn to the right of each image. The South Pole Station and the ASI field of view at 557.7 nm are given by the small and large white circles, respectively.

2.3. IMAGE FUV Observation of Shock Aurora

[15] In this study, the global view of the shock aurora in the Southern Hemisphere was identified by the Wideband Imaging Camera (WIC) and the Spectrographic Imager with two channels at 121.8 nm (SI12) and 135.6 nm (SI13) of the IMAGE-FUV. The WIC has a passband between 140 and 180 nm. It is mostly sensitive to the LBH bands and the NI 149.3 nm line, but also includes a small contribution from the NI 174.3 nm and OI 135.6 nm lines. Excitation of the LBH bands and NI lines is produced by incident primary electrons, protons and secondary electrons colliding with N_2 molecules. The SI12 is sensitive to the Doppler-shifted Lyman-α emission associated with proton aurora. The SI13 has a passband of $\sim$5 nm centered on the 135.6 nm OI emission line, which is mostly sensitive to electron aurora. Temporal resolution of three simultaneous snapshots obtained with the WIC, SI12, and SI13 is about 2 min. In the presentation of our data we have not made the appropriate subtraction from the WIC/SI13 data to remove the proton-produced emissions.

[16] Figure 3 shows sequence of the WIC images from the Southern Hemisphere displayed on a MLAT/MLT grid from 1834:04 UT to 1852:50 UT, observed by the IMAGE-FUV. The emission height is taken to be 130 km. The smaller circle is a location of SPA. The larger circle is the ASI field of view at 557.7 nm when assuming the main emission height to be 120 km.

[17] Figure 3a presents the quiet precondition on the dayside just before the arrival of IP shock. The very weak auroral emissions on the dayside were observed around $-77°$. The initial auroral response to the IP shock on the dayside ionosphere was observed at 1836:09 UT (Figure 3b) over a localized area in the prenoon region (9.0–12.0 MLT and $-77°$ to $-78°$ MLAT). In Figure 3c, the prenoon auroral emission was more enhanced (more than $\sim$0.6 kR) and the brightening area expanded to dawnside as well as to duskside (6.0–15.0 MLT). In addition to the high-latitude auroral emission, another dayside emission induced by the IP shock was seen equatorward of the main auroral oval (9.0–15.0 MLT and $-65°$ to $-68°$ MLAT), such as in the subauroral zone. The SI12 (proton aurora) also observed the dayside subauroral emission with stronger intensity, as shown later. The subauroral emission is well similar to the shock-induced subauroral emissions mainly due to precipitating protons, reported by several authors [*Liou et al.*, 2002; *Hubert et al.*, 2003]. About 5 min (Figure 3d) after SC onset, the high-latitude auroral emission displayed a dawn-dusk asymmetry. The extension of the auroral emission reached the nightside sector in dawn, while in dusk it reached only the $\sim$17.0 MLT. The dawn-dusk asymmetry in the auroral extension was seen also in the SI12 image (not shown), but opposite to that of the WIC image (i.e., the proton emission in dusk was more extended to the nightside sector than that in dawn). At the same time, the dayside subauroral emission slightly shifted equatorward with decreasing intensity.

[18] About 7 min (Figure 3e) after the SC onset, the auroral oval was almost symmetric, although the dawnside width was wider. The dayside subauroral emission almost disappeared in the WIC field of view. The significant precipitation on the dawnside was seen on the nightside (3.0–5.0 MLT), rather than on the dayside. On the other hand, the afternoon precipitation was enhanced in a narrow latitude range of $-73°$ to $-75°$ MLAT (around the middle of the oval) in the 14.0–20.0 MLT sector. At this time, the afternoon auroral oval just came into the field of view of the ASI images, presented in next section. The intensity in the ASI field of view exceeded 1.0 kR. After that (Figures 3f–3i), the duskside brightest region shifted gradually to the nightside sector ($\sim$20 MLT) with increasing the intensity, and finally it passed out of the ASI field of view. The propagation speed is about 8–10 km/s. At 1852:50 UT (Figure 3j), the intensity of the whole oval slightly weakened, except for the midnight auroral activity.

[19] About 20 min before the onset of the dayside shock aurora presented above, a localized auroral bright spot in the postmidnight sector was detected with the WIC at $\sim$1817 UT (not shown). The bright spot was centered at $\sim$02 MLT and $-70°$ MLAT. Until $\sim$1840 UT, the center of the midnight bright spot moved longitudinally from the $\sim$2.0 MLT to $\sim$0.0 MLT sector, and the central emissions

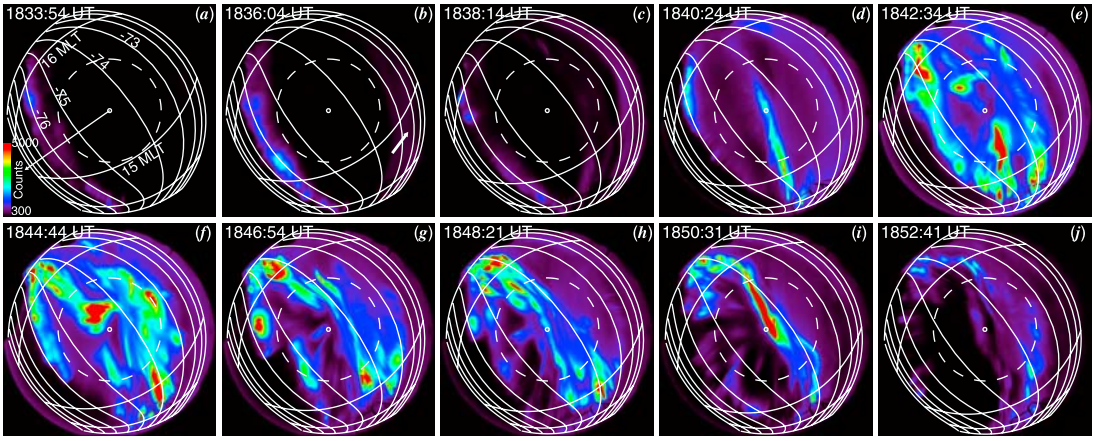

Figure 4. Sequence of all-sky images at 557.7 nm taken with the ASI at the South Pole Station. Selected geomagnetic latitude and MLT grid curves are overplotted. The direction to the magnetic pole is marked by thin arrow. Each image is shown at the nearest time to each WIC image shown in Figure 3. Thick arrow in Figure 4b shows the initial brightening of diffuse emission.

showed quasi-periodic intensifications. The midnight bright spots took place during the weak southward IMF of 0.0 to −1.0 nT. The behaviors of the dynamic bright spots in the midnight sector are well similar to those of a typical pseudobreakup [e.g., *Pulkkinen et al.*, 1998; *Zhou and Tsurutani*, 2001]. Pseudobreakups are often accompanied by substorm-like magnetospheric disturbances (such as magnetospheric reconnection in the tail, dipolarization of the geomagnetic field, disruption of the tail current, and dispersionless particle injection), but their scales are somewhat small or localized. At ∼1838 UT (corresponding to about 3 min after the SC onset), the midnight bright area slightly thickened with intensifying the brightness, as seen in Figure 3c. After that (see Figures 3e–3i), the midnight bright area extended westward (premidnight sector). Moreover, the magnetic H component at a station conjugated with the midnight auroral activity started decreasing at ∼1838 UT and reached about −200 nT in ∼6 min (not shown). The auroral bulge-/surge-like development and the moderate magnetic negative bay in the night sector are often regarded as the indications of substorm, although the auroral expansion in latitude/longitude was small and its intensity was weak. For our event, it seemed that the substorm onset began ∼3 min after the SC onset. However, we are not sure whether or not the substorm was actually triggered by the IP shock, because various external triggering mechanisms for substorms are suggested [*Zhou and Tsurutani*, 2001; *Tsurutani and Zhou*, 2003; *Liou et al.*, 2003, and references therein]. The more detailed characteristics of the pseudobreakup/substorm and the possible mechanisms are beyond the scope of this paper and will be discussed in a separate paper in the future.

2.4. ASI Observation of Shock Aurora

[20] Figures 4 and 5 show sequences of 557.7 nm and 630.0 nm images observed by the All-Sky Imager (ASI) at the South Pole Station (SPA), respectively. Each of the ASI images is selected at the closest time to each of the WIC images presented in Figure 3. Contours of MLATs and MLTs are overplotted on each ASI image. The center circle is the zenith of SPA and the dashed circle is the geographic latitude of −89°. During this event, it took about 43 s to complete the exposure of the three interference filters. It is

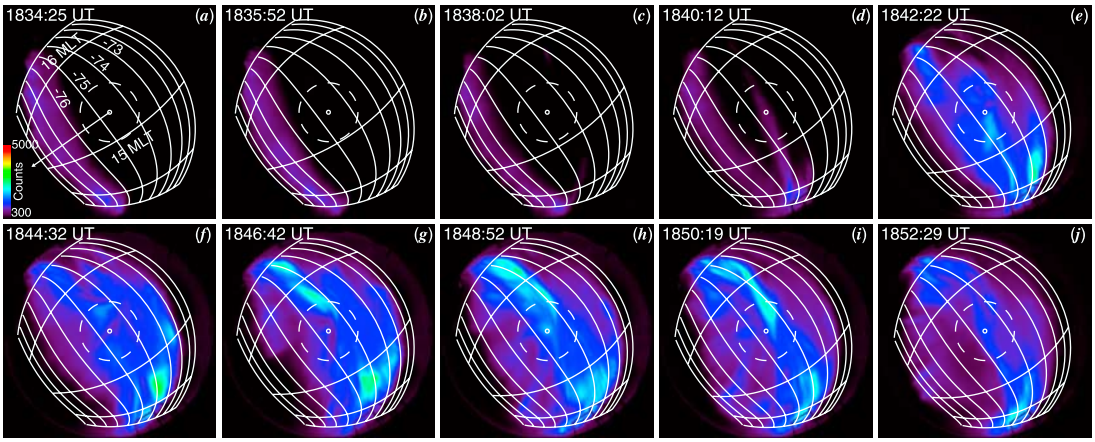

Figure 5. The same format as Figure 4, but for the 630.0 nm ASI images.

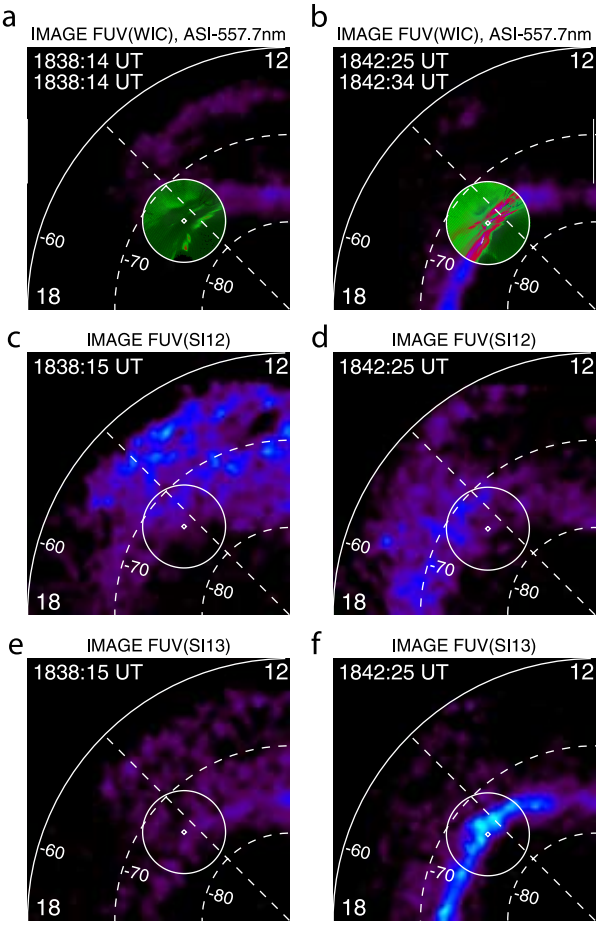

Figure 6. (a and b) An overview of the 557.7 nm ASI image remapped on the WIC image in the afternoon sector at the nearest time of the observed diffuse- (Figure 6a) and discrete- (Figure 6b) type shock aurora, as seen in Figures 4c and 4e, respectively. (c and d) The SI12 image and (e and f) the SI13 image. The color scale of each IMAGE-FUV image is the same as that of Figure 3.

generally considered that the 557.7 nm emission results from neutral atomic oxygen excited directly and/or indirectly by precipitating keV electrons, and that the expected peak altitude of the emission is around 120 km. On the other hand, the 630.0 nm emission also results from neutral atomic oxygen, but excited by precipitating soft electrons (mainly less than 1 keV). The expected peak altitude of the 630.0 nm emission is somewhat higher than that of the 557.7 nm emission (in this study, it was assumed as 250 km). Temporal evolution of the shock aurora seen by the ASI are almost similar to that seen by the WIC in the ASI field of view (from −69° to −78° MLAT in the 14–17 MLT sector), but the ASI enable us to identify more detailed structures of the dayside shock aurora.

[21] In the first ASI image at 557.7 nm (Figure 4a; before the SC onset), we found the quiet auroral emission lying between −76° and −77° MLAT, corresponding to the postnoon main oval with the narrow and weak emissions presented in Figure 3a. The first 630.0 nm image (Figure 5a) indicated the quiet auroral emission at latitudes overlapping with the 557.7 nm emission. The intensity of the 630.0 nm emission was roughly comparable to that of the 557.7 nm emission. In the postnoon main oval, periodic spot-like auroral brightenings at 557.7nm often appeared before the SC (not shown), although some of them remained just after the SC. At 1836:04 UT (Figure 4b) when the first emission of the dayside shock aurora was detected by the WIC, the first brightening at 557.7 nm in response to the IP shock in the ASI field of view appeared around −73° MLAT in the 14.0–15.0 MLT sector (shown by thick arrow). The auroral brightening was weak in intensity and less structured. Therefore, this aurora was categorized as diffuse. At 1838:14 UT (Figure 4c), the diffuse-type aurora expanded equatorward (−70° MLAT) and tailward (near the 16.0 MLT sector). The tailward propagation speed of the eastern edge was 5–8 km/s on average. During the shock-induced diffuse emission at 557.7 nm, no any apparent enhancement of auroral emission at 630.0 nm was found in this region (Figures 5b and 5c).

[22] At 1840:24 UT (Figure 4d), in addition to further intensification of the diffuse auroral emission at 557.7 nm, a newly developing auroral arc across the zenith began to appear between 14.0 and 15.5 MLT. However, there was no counterpart in the corresponding WIC image (Figure 3d). The intensity of the auroral arc emission was stronger than that of the surrounding diffuse auroral emission. The corresponding arc was observed also at 630.0 nm (Figure 5d), although the structure was less sharp. The appearance of this arc was consistent with the increasing 630.0 nm emission after 1840 UT detected by the photometer at SPA. After 1842 UT (Figures 4e–4i), the highly structured auroral emission at 557.7 nm was predominant in the ASI field of view. The discrete aurora emissions developed with changing the forms in ranges of −73° to −76° MLAT and of 14.0 to 17.0 MLT. The developing arcs at 557.7 nm roughly coincided with those at 630.0 nm, but some structures at 630.0 nm were indistinct or absent because of the longer lifetime of the emission (Figures 5e–5i). The main part of the discrete auroral emission also moved tailward. About 13 min after the initial brightening of the discrete-type shock aurora, the auroral intensity slightly weakened (Figures 4j and 5j).

[23] The SI12 and SI13 provide us with information about relative contribution of precipitating protons and electrons in the diffuse/discrete-type shock aurora observed with the ASI. Figure 6 shows an overview of the 557.7 nm ASI image remapped on the WIC image in the afternoon sector at the nearest time of the observed diffuse- (Figure 6a) and discrete- (Figure 6b) type shock aurora seen in Figures 4c and 4e, respectively. Figures 6c and 6d show the SI12 image, and Figures 6e and 6f show the SI13 image at each time. As mentioned in section 2.3, it is found that the proton precipitation played a major role in the shock-induced dayside subauroral emission. As seen in Figure 6 (left), in the diffuse 557.7 nm shock aurora (light green area in Figure 6a) expanding equatorward of the oval (−70° to −73°) at 1838 UT, the emission of the SI12 image (∼0.7 kR on an average) was much stronger than that of the SI13 image (∼0.32 kR). In Figure 6 (right), on the other hand, we found that the location of the discrete auroral emission (red area of Figure 6b) detected by the ASI at 1842 UT exactly

corresponded to the brighter area in the middle of the afternoon auroral oval detected by the WIC/SI13 (more than 1.0 kR). In comparison with the diffuse aurora, the proton contribution in the discrete aurora was relatively small.

3. Discussion and Conclusions

[24] The FUV-WIC images showed a clear dawn-dusk asymmetry in expansion of the dayside shock aurora during the initial interval (1836–1840 UT) after the SC onset. As seen in Figure 3, the auroral extension from the first emission region (prenoon) to the dawn-dusk terminator was faster in the dawn sector than in the dusk sector. Similar dawn-dusk asymmetry in the shock aurora has been reported by previous studies based on the Polar UVI [*Zhou and Tsurutani*, 1999] and IMAGE FUV-WIC [*Meurant et al.*, 2004] instruments. For our event, the shock aurora in the morning sector expanded within about 4 min from the prenoon to the nightside sector. The western edge of the shock aurora reached the ~9.0 MLT sector at 1836:09 UT and the ~6.0 MLT sector at 1838:14 UT. Assuming −75° MLAT as an average latitude, the average longitudinal speed is ~11 km/s, comparable to that estimated by *Zhou and Tsurutani* [1999]. The propagation speed in the polar ionosphere could correspond to that of the IP shock traveling along the magnetopause flank. During the same interval, the SI12 indicated the opposite dawn-dusk asymmetry (faster extension in dusk) in the proton aurora. As mentioned above, for this event the pseudobreakup activity in the postmidnight sector preceded the shock aurora. Pseudobreakups are often accompanied by a localized injection of electrons/ions with a few keV [*Yahnin et al.*, 2001]. If such particle injection took place in the postmidnight, it is expected that a drifting/trapped electron (proton) population might be distributed mainly in the dawnside (duskside) as a preconditioning of the magnetosphere before the SC. Basically, the averaged energetic electron (proton) population tends to be abundant on the dawnside (duskside) rather than the duskside (dawnside), even if the magnetosphere is quiet [*Hardy et al.*, 1987]. In either case, it is likely that the faster extension of the electron (proton) shock aurora in the morning (afternoon) sector is linked to the shock-induced precipitation of the drifting/trapped energetic particles. It is suggested that the precipitation is probably caused by adiabatic compression [*Zhou and Tsurutani*, 1999] and/or reductions in the mirror ratio [*Liou et al.*, 2002] induced by the Psw-induced magnetospheric compression. If so, the morning shock aurora form detected by the WIC is expected to be diffuse.

[25] In the afternoon sector, the ground-based optical observations can confirm development of two different types of shock aurora, diffuse and discrete. Before ~1840 UT, we found that the afternoon shock aurora detected by the WIC was of diffuse type and appeared mainly equatorward (−70° to −73° MLAT) of the ASI field of view. The diffuse-type shock aurora was detected only at 557.7 nm (no signature at 630.0 nm) and its eastern edge propagated tailward by a speed of 5–8 km/s. As shown in Figure 6 (left), the SI12 and SI13 images indicated proton precipitation in the diffuse 557.7 nm emission was much stronger than electron precipitation. Several previous authors reported that proton precipitation contributes to the optical emissions at the major electron auroral lines, such as 557.7 nm, 427.8 nm, and 630.0 nm [e.g., *Srivastava and Singh*, 1988; *Rees*, 1989; *Lummerzheim et al.*, 2001]. It is thought that the auroral emissions are contributed from the secondary electrons under proton precipitation [*Rees*, 1989]. According to the model prediction of *Srivastava and Singh* [1988], if the proton contribution were significant in the diffuse 557.7 nm emission, the characteristic proton energy might be more than 10 keV because the diffuse emission was detectable only at 557.7 nm. Our results suggest that the preceding diffuse-type shock aurora in the afternoon sector was caused by precipitation of keV protons as well as electrons, entering the loss cone as the result of the shock-induced magnetic field and plasma compression of the outer magnetosphere.

[26] At ~1840 UT (Figures 4d and 5d), in addition to further enhancement of the diffuse-type shock aurora at 557.7 nm, a new discrete-type shock aurora began to appear near the zenith in the ASI field of view. The discrete arc was seen at both 557.7 nm and 630.0 nm. The highly structured auroral forms (like multiple fan arcs) dynamically changed and the major emissions propagated eastward (tailward). The significant discrete-type shock aurora was located between −73° and −76° MLAT, exactly corresponding to the stronger auroral emission in the middle of the afternoon oval observed by the WIC/SI13 (see Figure 6, right). The SI12 indicated that proton precipitation had little contribution in the discrete aurora emission. Therefore, the discrete-type shock aurora results from intense precipitation of electrons, rather than protons.

[27] The characteristic electron energy producing the discrete shock aurora can be speculated from the emission ratio of different filters on the basis of the numerical model results by *Rees and Luckey* [1974]. During the discrete-type shock aurora the 630.0/427.8 ratio estimated from the photometer data at SPA was 0.5~1.0, roughly corresponding to electrons in a few keV or less energy range. The contribution of lower-energy (less than 1 keV) electrons to the discrete-type shock aurora is indirectly supported also by the 630.0 nm ASI images. The precipitating lower-energy electrons in the afternoon shock aurora were reported by the previous studies using direct in situ satellite observations [*Meurant et al.*, 2003; *Zhou et al.*, 2003]. They demonstrated that the precipitating lower-energy electrons are highly structured and predominant at higher latitudes (~75° or more MLAT). The precipitation of the highly structured lower-energy electrons via some field-aligned acceleration processes is generally believed to cause the discrete auroral emission as seen in the present study.

[28] Some possible mechanisms of the Psw-induced field-aligned currents (FACs) at the magnetopause were discussed by *Zhou et al.* [2003]. For our event, however, the main location of the discrete forms was in the middle of the auroral oval observed with the WIC, not at the poleward edge. This implies that the Psw-induced FACs originate from somewhere inside the magnetosphere, rather than at the magnetopause. Therefore, we can rule out any mechanism that is based on the Psw-induced FAC generation at the magnetopause. *Kozlovsky et al.* [2005] recently proposed another mechanism of the FAC generation to explain westward/poleward motions of Psw-induced prenoon arcs.

However, such an explanation cannot apply to our observations because the polarity and motion of the Psw-induced FACs predicted by *Kozlovsky et al.* [2005] do not match development of the afternoon discrete auroral forms presented here.

[29] As the most plausible mechanism for this case study, the afternoon discrete-type shock aurora, if not all, may be associated with generation of upward FACs for the main impulse (MI) of SC. During the interval when the discrete-type shock aurora was predominant, the geomagnetic H component at SPA showed the MI of SC. It is well known that the MI-related FACs consist of a pair of downward current on the dawnside and upward one on the duskside [*Araki*, 1994]. Under the large-scale MI-related FAC structure, one can expect that the discrete-type shock auroral emissions are more detectable on the duskside than the dawnside. Using a numerical simulation, *Fujita et al.* [2003] investigated the three-dimensional current circuit associated with MI. They demonstrated that the MI-related upward FAC first appears in the postnoon polar ionosphere ($\sim$70°, $\sim$13 MLT) about 3–4 min after the arrival of a Psw enhancement at the subsolar point, and then move to the dusk terminator with increasing the intensity. During this period, the center of the upward FAC around 15 MLT is 73°–75°. The temporal and spatial variations of the discrete-type shock auroral emission presented here are well similar to those of the upward FAC. This suggests that the afternoon discrete-type shock aurora appears coincident with the MI-related FAC developing after passage of a fast-mode shock. According to their simulation results, the MI-related FAC system originates around the inner edge of an enhanced pressure region well inside the magnetosphere, not just inside the magnetopause. This is in better agreement with our result that the afternoon discrete emission was seen in the middle of the oval. Also, the FAC system appears to be connected with the current generator in the cusp region through the off-equatorial plane (Figure 10 of *Fujita et al.* [2003]).

[30] The observed discrete auroral emission had small-scale fine structures (multiple arcs) varying dynamically in both space and time. Probably, the individual arcs could be associated with highly structured FACs embedded in the large-scale upward FAC system for MI. If the ionosphere was nonuniform in conductivity and electric field via various physical processes in the magnetosphere (generation of additional Alfven waves), the ionosphere would play a passive role in the formation of multiple auroral structures, as demonstrated by *Zhu et al.* [2005]. The small magnetic field perturbation superposed on the MI signature at SPA (see Figure 2, top) might be a manifestation of the additional Alfven waves. However, further observational and numerical investigations are required to establish generation mechanism responsible for the multiple small-scale structures of shock aurora.

[31] It is well known that IMF changes lead to discrete arcs (precipitation of accelerated electrons) on the dayside, especially around the ionospheric foot points of large-scale upward FACs [cf. *Newell et al.*, 1996]. During the discrete-type shock aurora seen in the afternoon sector, the IMF underwent a short-time ($\sim$3 min) southward excursion with $\sim$−3 nT about 7 min after the IP shock. The southward IMF excursion was accompanied by a small Psw increase (from $\sim$5 to 6 nPa). The ground response to the small Psw increase indicated a small positive change of the magnetic H component at Kakioka between 1848 and 1853 UT (Figure 2, bottom). This result implies that, if the effect of the IMF change appears on the polar ionosphere, it is $\sim$8 min after the appearance of the discrete-type shock aurora, or later. Therefore, the weak southward IMF excursion was not likely a direct cause triggering the present discrete aurora, although its effect might somewhat be superposed on the developing discrete-type shock aurora.

[32] We presented a case study of a postnoon shock aurora event that occurred on 14 June 2005, on the basis of simultaneous ground-satellite optical observations. To our knowledge, such an opportunity of observing the dayside shock aurora is extremely rare, except for *Kozlovsky et al.* [2005]. Simultaneous optical observations from ground and space provided good similarities for spatial/temporal evolution of the shock aurora. Especially, the ASI observations at SPA allow us to identify when and where diffuse- and discrete-type shock auroral forms develop in the afternoon sector. The major findings of the postnoon shock aurora for this case study are as follows: (1) two-step development of the postnoon shock aurora (the diffuse-type shock aurora first appeared and expanded, and $\sim$5 min later the discrete-type one began to develop), (2) the diffuse-type shock aurora was detectable only at 557.7 nm equatorward of the oval (−70° to −73° MLAT), while the discrete-type one at both 557.7 nm and 630.0 nm in the middle of the oval (−73° to −76° MLAT), (3) relative contribution of proton versus electron precipitation to each shock auroral form, and (4) the discrete-type shock aurora coincided with the MI of SC. Identifying temporal/spatial features of both shock auroral forms is very important to clarify the predominant precipitation mechanism(s) of nonaccelerated or accelerated particles in the developing shock aurora. The two-step development of the observed postnoon shock aurora suggests that shock-induced precipitation mechanisms are a two-step process.

[33] **Acknowledgments.** The Japanese ASI project at the South Pole Station was initiated by M. Ejiri and S. Okano, and performed under an agreement of cooperation between National Institute of Polar Research and the United States National Science Foundation. We would like to thank winter-over science technicians at the South Pole Station for maintaining the instruments. We gratefully acknowledge National Science Foundation grant ANT 0638587 to Siena College. ACE level 2 data were provided through the CDA Web site. The SYM-H index and Kakioka magnetometer data were provided by World Data Center for Geomagnetism at Kyoto University, Japan.

[34] Wolfgang Baumjohann thanks the reviewers for their assistance in evaluating this paper.

References

Araki, T. (1994), A physical model of geomagnetic sudden commencement, in *Solar Wind Sources of Magnetospheric Ultra-Low-Frequency Waves*, *Geophys. Monogr. Ser.*, vol. 81, edited by M. J. Engebretson, K. Takahashi, and M. Scholer, 183 pp., AGU, Washington, D. C.

Chua, D., G. Parks, M. Brittnacher, W. Peria, G. Germany, J. Spann, and C. Carlson (2001), Energy characteristics of auroral electron precipitation: A comparison of substorms and pressure pulse related auroral activity, *J. Geophys. Res.*, *106*, 5945, doi:10.1029/2000JA003027.

Colburn, D. S., and C. P. Sonett (1966), Discontinuities in the solar wind, *Space Sci. Rev.*, *5*, 439, doi:10.1007/BF00240575.

Craven, J. D., L. A. Frank, C. T. Russell, E. E. Smith, and R. P. Lepping (1986), Global auroral responses to magnetospheric compressions by shocks in the solar wind: Two case studies, in *Solar Wind-Magnetosphere Coupling*, edited by Y. Kamide and J. A. Slavin, 367 pp., Terra Sci., Tokyo.

Ebihara, Y., Y. M. Tanaka, S. Takasaki, A. T. Weatherwax, and M. Taguchi (2007), Quasi-stationary auroral patches observed at the South Pole Station, *J. Geophys. Res.*, *112*, A01201, doi:10.1029/2006JA012087.

Fujita, S., T. Tanaka, T. Kikuchi, K. Fujimoto, and M. Itonaga (2003), A numerical simulation of the geomagnetic sudden commencement: 2. Plasma processes in the main impulse, *J. Geophys. Res.*, *108*(A12), 1417, doi:10.1029/2002JA009763.

Hardy, D. A., M. S. Gussenhoven, R. Raistrick, and W. J. McNeil (1987), Statistical and functional representations of the pattern of auroral energy flux and conductivity, *J. Geophys. Res.*, *92*, 12,275, doi:10.1029/JA092iA11p12275.

Hubert, B., J. C. Gérard, S. A. Fuselier, and S. B. Mende (2003), Observation of dayside subauroral proton flashes with the IMAGE-FUV imagers, *Geophys. Res. Lett.*, *30*(3), 1145, doi:10.1029/2002GL016464.

Iyemori, T. (1990), Storm-time magnetospheric currents inferred from mid-latitude geomagnetic field variation, *J. Geomag. Geoelectr.*, *42*, 1249.

Kozlovsky, A., V. Safargaleev, N. Østgaard, T. Turunen, A. Koustov, J. Jussila, and A. Roldugin (2005), On the motion of dayside auroras caused by a solar wind pressure pulse, *Ann. Geophys.*, *23*, 509.

Laundal, K. M., and N. Østgaard (2008), Persistent global proton aurora caused by high solar wind dynamic pressure, *J. Geophys. Res.*, *113*, A08231, doi:10.1029/2008JA013147.

Liou, K., C.-C. Wu, R. P. Lepping, P. T. Newell, and C.-I. Meng (2002), Midday sub-auroral patches (MSPs) associated with interplanetary shocks, *Geophys. Res. Lett.*, *29*(16), 1771, doi:10.1029/2001GL014182.

Liou, K., P. T. Newell, C.-I. Meng, C.-C. Wu, and R. P. Lepping (2003), Investigation of external triggering of substorms with Polar ultraviolet imager observations, *J. Geophys. Res.*, *108*(A10), 1364, doi:10.1029/2003JA009984.

Liou, K., P. T. Newell, J.-H. Shue, C.-I. Meng, Y. Miyashita, H. Kojima, and H. Matsumoto (2007), "Compression aurora": Particle precipitation driven by long-duration high solar wind ram pressure, *J. Geophys. Res.*, *112*, A11216, doi:10.1029/2007JA012443.

Lummerzheim, D., M. Galand, J. Semeter, M. J. Mendillo, M. H. Rees, and F. J. Rich (2001), Emission of OI (630 nm) in proton aurora, *J. Geophys. Res.*, *106*, 141, doi:10.1029/2000JA002005.

Mende, S. B., et al. (2000), Far ultraviolet imaging from the IMAGE spacecraft, 1, System design, *Space Sci. Rev.*, *91*, 243, doi:10.1023/A:1005271728567.

Meurant, M., J.-C. Gérard, B. Hubert, V. Coumans, C. Blockx, N. Østgaard, and S. B. Mende (2003), Dynamics of global scale electron and proton precipitation induced by a solar wind pressure pulse, *Geophys. Res. Lett.*, *30*(20), 2032, doi:10.1029/2003GL018017.

Meurant, M., J.-C. Gérard, C. Blockx, B. Hubert, and V. Coumans (2004), Propagation of electron and proton shock-induced aurora and the role of the interplanetary magnetic field and solar wind, *J. Geophys. Res.*, *109*, A10210, doi:10.1029/2004JA010453.

Moore, T. E., D. L. Gallagher, J. L. Horwitz, and R. H. Comfort (1987), MHD wave breaking in the outer plasmasphere, *Geophys. Res. Lett.*, *14*, 1007, doi:10.1029/GL014i010p01007.

Newell, P. T., K. M. Lyons, and C.-I. Meng (1996), A large survey of electron acceleration event, *J. Geophys. Res.*, *101*, 2599, doi:10.1029/95JA03147.

Pulkkinen, T. I., D. N. Baker, M. Wiltberger, C. Goodrich, R. Lopez, and J. Lyon (1998), Pseudobreakup and substorm onset: Observations and MHD simulations compared, *J. Geophys. Res.*, *103*, 14,847, doi:10.1029/97JA03244.

Rees, M. H. (1989), Antarctic upper atmosphere investigations by optical methods, *Planet. Space Sci.*, *37*, 95, doi:10.1016/0032-0633(89)90050-0.

Rees, M. H., and D. Luckey (1974), Auroral electron energy derived from ratio of spectroscopic emissions: 1. Model computations, *J. Geophys. Res.*, *79*, 5181, doi:10.1029/JA079i034p05181.

Sandholt, P. E., A. Egeland, J. A. Holtet, B. Lybekk, K. Svenes, and S. Åsheim (1985), Large- and small-scale dynamics of the polar cusp, *J. Geophys. Res.*, *90*, 4407, doi:10.1029/JA090iA05p04407.

Sandholt, P. E., et al. (1994), Cusp/Cleft auroral activity in relation to solar wind dynamic pressure, interplanetary magnetic field Bz and By, *J. Geophys. Res.*, *99*(A9), 17,323, doi:10.1029/94JA00679.

Spann, J. F., M. Brittnacher, R. Elsen, G. A. Germany, and G. K. Parks (1998), Initial response and complex polar cap structures of the aurora in response to the January 10, 1997 magnetic cloud, *Geophys. Res. Lett.*, *25*, 2577, doi:10.1029/98GL00647.

Srivastava, V., and V. Singh (1988), Model calculations of O (^{1}S) and O (^{1}D) emissions under proton bombardment, *J. Geophys. Res.*, *93*, 5855, doi:10.1029/JA093iA06p05855.

Tsurutani, B. T., and X.-Y. Zhou (2003), Interplanetary shock triggering of substorms: WIND and Polar, *Adv. Space Res.*, *31*, 1063, doi:10.1016/S0273-1177(02)00796-2.

Tsurutani, B. T., et al. (2001), Auroral zone dayside precipitation during magnetic storm initial phases, *J. Atmos. Sol. Terr. Phys.*, *63*, 513, doi:10.1016/S1364-6826(00)00161-9.

Vorobyev, V. G. (1974), SC-associated effects in auroras, *Geomagn. Aeron.*, *14*, 72.

Yahnin, A. G., et al. (2001), Correlated Interball/ground-based observations of isolated substorm: The pseudobreakup phase, *Ann. Geophys.*, *19*, 687.

Zhou, X.-Y., and B. T. Tsurutani (1999), Rapid intensification and propagation of the dayside aurora: Large scale interplanetary pressure pulses (fast shocks), *J. Geophys. Res.*, *26*, 1097, doi:10.1029/1999GL900173.

Zhou, X.-Y., and B. T. Tsurutani (2001), Interplanetary shock triggering of nightside geomagnetic activity: Substorm, pseudobreakup, and quiescent events, *J. Geophys. Res.*, *106*, 18,957, doi:10.1029/2000JA003028.

Zhou, X.-Y., R. J. Strangeway, P. C. Anderson, D. G. Sibeck, B. T. Tsurutani, G. Haerendel, H. U. Frey, and J. K. Arballo (2003), Shock aurora, FAST and DMSP observations, *J. Geophys. Res.*, *108*(A4), 8019, doi:10.1029/2002JA009701.

Zhu, L., J. J. Sojka, and R. W. Schunk (2005), Active ionospheric role in small-scale aurora structuring, *J. Atmos. Sol. Terr. Phys.*, *67*, 687, doi:10.1016/j.jastp.2004.12.004.

Y. Ebihara, Institute for Advanced Research, Nagoya University, Nagoya 464-8601, Japan.

H. U. Frey, Space Sciences Laboratory, University of California, Berkeley, CA 94720, USA.

A. Kadokura, T. Motoba, and N. Sato, National Institute of Polar Research, Tokyo 190-8518, Japan. (motoba.tetsuo@nipr.ac.jp)

A. T. Weatherwax, Department of Physics, Siena College, Loudonville, NY 12211, USA.